The Computational Post Buckling Analysis Of Fuselage Stiffened Panels Loaded In Compression

Lynch, C., Murphy, A., Price, M., & Gibson, A. (2004). The Computational Post Buckling Analysis Of Fuselage Stiffened Panels Loaded In Compression. *Thin-Walled Structures*, *42(10)*(10), 1445-1464. https://doi.org/10.1016/j.tws.2004.04.002

Published in:
Thin-Walled Structures

Document Version:
Peer reviewed version

Queen's University Belfast - Research Portal:
Link to publication record in Queen's University Belfast Research Portal

THE COMPUTATIONAL POST BUCKLING ANALYSIS OF FUSELAGE STIFFENED PANELS LOADED IN COMPRESSION

A. Murphy[+], C. Lynch[*], M. Price, A. Gibson

School of Aeronautical Engineering, Queen's University Belfast, Belfast, N. Ireland

* Timoney Group, Gibbstown, Navan, Co. Meath, Ireland

+ Corresponding author: *Email:* a.murphy@qub.ac.uk *Fax:* +44 (028) 9038 2701

Abstract

Fuselage panels are commonly fabricated as skin-stringer constructions, which are permitted to locally buckle under normal flight loads. The current analysis methodologies used to determine the post buckling response behaviour of stiffened panels relies on applying simplifying assumptions with semi-empirical / empirical data. Using the Finite Element method and employing non-linear material and geometric analysis procedures it is possible to model the post buckling behaviour of stiffened panels without having to place the same emphases on simplifying assumptions or empirical data. Investigation of element, mesh, idealisation, imperfection and solution procedure selection is been undertaken, with results validated against mechanical tests. The research undertaken has demonstrated that using a commercial implicit code, the Finite Element method can be used successfully to model the post buckling behaviour of flat riveted panels. The work has generated a series of guidelines for the non-linear computational analysis of flat riveted panels subjected to uniform axial compression.

Keywords: Fuselage buckling analysis, Post buckling analysis, Non-linear Finite Element modelling, Stiffened panel compression testing.

1. Introduction

1.1. Background

In order to maximise the strength to weight ratio of fuselage stiffened panels, it is necessary to allow the skin in between stiffeners to buckle below the ultimate failure load. This buckling skin arrangement offers notable weight savings over non buckling designs [1]. A typical load ratio of a third local skin buckling load to ultimate failure load is common for commercial aircraft [2]. The ability to accurately predict the local buckling, post buckling and failure behaviour of stiffened panel designs is therefore essential for aircraft structures. The conventional analysis methodologies used to determine the buckling and post buckling response behaviour involves empirical and semi empirical plate and column design formulae [3-6]. The formulae are extended to cover stiffened panel analysis by applying simplifying assumptions, which allow the division of the stiffened panel structure into sub-members, plates and columns, and assuming sub-member boundary conditions. The empirical data, simplifying assumptions and conservative boundary conditions result in a lower bound analysis, which may lead to over-designed structures.

1.2. Conventional Fuselage Panel Design

In conventional fuselage design, the stress distribution throughout the structure is typically obtained from linear static Finite Element analyses for a variety of loadcases. For each loadcase, the stresses in the individual members are compared to appropriate allowable stresses giving a margin of safety for each member. The stresses in the skin panels are compared to theoretical plate buckling stresses considering both compression and shear loading. Fig. 1 depicts a typically skin panel bounded by stringer and frames, the buckling of this skin panel is very complex due to the interactions between the skin and stringers, the skin and frames and the stringers and frames. However, the conventional analysis makes a number of simplifying assumptions, first the plate width, b, is defined as the distance between stringer rivet lines, Fig. 1, the plate length, a, is taken to be the distance between frame rivet lines, finally the plate is assumed to be simply-supported along all four edges. The skin allowable stress is calculated using the plate buckling formula, equation (1)

developed by Timoshenko [7]. The buckling coefficient, k, is a function of the plate aspect ratio and the plate loading (shear or compression) [6].

$$\sigma_{skin} = \frac{\pi^2 \cdot k \cdot E_T}{12\left(1-\nu^2\right)}\left(\frac{t}{b}\right)^2 \quad (1)$$

To account for post-yield material behaviour the skin tangent modulus is used, E_T, with a Ramberg-Osgood [8] definition of the material stress-strain behaviour assumed.

The stresses in the stringers are compared to the column buckling stresses for flexural, torsional, local-flexural, local-torsional buckling modes; again this involves a number of simplifying assumptions. First, to account for local skin buckling it is assumed an effective width of skin works with the stringer within the post buckling range. Second, the stringer plus effective skin are assumed to act as a strut of length equal to the panel frame pitch, L, simply-supported at both ends. The stringer allowable stress for local-flexural buckling, the mode which dominates the panel geometry studied herein, is given by the secant formula, equation (2).

$$\sigma_{str.max} = \sigma_{str.ave}\left[1+\frac{ey}{\rho^2}\sec\left(\frac{L}{2\rho}\sqrt{\frac{\sigma_{str.ave}}{E_T}}\right)\right] \quad (2)$$

The equation gives the maximum compressive stress, $\sigma_{str.max}$, in the column as a function of the average compression stress, $\sigma_{str.ave}$, the eccentricity ratio, ey/ρ^2, the slenderness ratio, L/ρ, and the tangent module, E_T. It should be noted that the moment of inertia of the cross-section and the cross-sectional area of the column use to calculate the radius of gyration of the cross-section include the effective skin material. Failure is assumed to occur when the maximum stress reaches some limiting value such as stringer or skin material yield stress or stringer element crippling stress.

1.3. Reducing Analysis Reliant on Design Formulae

This current work presents a Finite Element modelling procedure for the post buckling analysis of conventional riveted fuselage panels, with the aim of reducing analysis reliant on empirical and

semi empirical design formulae. The developed modelling methods focus on panel idealisation as well as element selection. The post buckling modelling techniques employ the commercial solver ABAQUS and the damped Newton-Raphson solution procedure. The developed modelling procedures are validated against a series of sub-panel and full-panel compression tests.

2. Computational Analysis

2.1. Element Selection

To enable element selection a mesh convergence study of the buckling and post buckling behaviour of a uniformly compressed simply supported square plate was undertaken. A problem for which the theoretical buckling and post buckling behaviour is well established [9]. Five different ABAQUS shell elements were considered. First, an eigenvalue buckling analyses was performed for a range of mesh densities to determine the first (fundamental) buckling mode and buckling stress. For each element model the fundamental buckling mode was used as an initial imperfection with a maximum magnitude of 10% of the skin thickness in a post buckling analysis, from which load-deflection curves were obtained. The performance of each element was assessed based on the convergence, with increasing mesh density, of the predicted buckling stresses and load-deflection curves to the corresponding theoretical behaviour. It was concluded, based on analysis results, that a second-order curved quadrilateral 8-noded thin shell element i.e. ABAQUS S8R5 element [10], provides optimum buckling and post buckling solutions, with four elements per buckle half-wavelength sufficient to obtain a high degree of accuracy.

2.2. Structural Idealisation

The idealisation approach adopted is similar to that of Domb et al. [11] in which the stringers are explicitly modelled using an assemblage of shell elements. This approach is essential to enable the buckling failure modes of the structure to be simulated. Domb modelled the riveted specimens as bonded structures, assuming a continuous connection at the skin-rivet-stringer interface. To investigate the accuracy of this assumption six different idealisations of the skin-rivet-stringer interface are examined, Fig. 2. In all six cases beam elements are used to model the stiffener bulbs,

the bulb beam elements are connected to the stringer web shell elements using rigid links. In method (a) the specimen is assumed to act as an integral structure with all nodes on the stringer flanges connected to the corresponding nodes on the skin using rigid links, as shown. Method (b) also models the interface as an integral joint, however here a single layer of shells is used to represent the combined skin and stringer flanges. These elements are given a layered composite section property which includes a layer of dummy material used to account for the offset between the skin and combined skin and stringer flanges, in a similar manner to the modelling approach applied by Domb et al [11].

The rivets are explicitly modelled and the contact conditions between the skin and stringer simulated in methods (c) and (d). In both these methods the mesh is generated such that adjacent nodes exist on the skin and stringer flanges at the rivet locations. These nodes are connected with rigid links in method (c). In method (d) a combination of spring elements is used to connect the nodes, with one spring element representing the axial stiffness and two spring elements representing the shear stiffness of the rivet. This is accomplished in ABAQUS with the flexible joint element, JOINTC, used to define the three spring elements at each rivet location. The contact conditions between the remaining nodes are represented using uni-axial gap elements, GAPUNI. Methods (e) and (f) are identical to methods (c) and (d) with the gap elements removed.

2.3. Material Properties

Compressive material properties obtained from coupon tests were used for all Finite Element analysis. Material test coupons were taken from the same material batches as the components from which the test validation specimens were manufactured. Material curves were incorporated into the Finite Element analysis models using the 'classical metal plasticity' constitutive theory available within the ABAQUS material library [10].

2.4. Solution Procedure

For each analysis model an initial eigenvalue analysis is performed to determine the fundamental buckling mode of the structure. The initial geometry is subsequently seeded with an imperfection in the shape of the fundamental buckling mode. Unless otherwise stated, the magnitude of this imperfection is 10% of the skin thickness, a value that is representative of typical imperfections present in conventional riveted fuselage structures. The post buckling analysis is then performed using the incremental-iterative Newton-Raphson solution procedure [11-13]. Within the Newton-Raphson solution procedure the structural problem is expressed as

$$[F] = [K_T][u] \tag{3}$$

where [F] are the applied loads and the tangent stiffness matrix $[K_T]$ is dependent on the displacement [u]. To determine the response of the structure to this applied loading the analysis is broken down into a series of load increments, one such load increment is illustrated in Fig. 3. At the start of the load increment (at u_0), the tangent stiffness K_{T0} is formed, from which the first displacement correction, Δu_a, is obtained using

$$[\Delta F] = [K_{T0}][\Delta u_a] \tag{4}$$

Using the displacement correction the structure's configuration is updated to u_a. The internal forces I_a (which are essentially the stresses integrated throughout the structure) are then determined in this updated configuration from which the force residual is calculated as

$$R_a = F_1 - I_a \tag{5}$$

For the structure to be in equilibrium the internal forces would be balanced by the external forces and hence the force residual would be zero. As this force residual will never be exactly zero, a force residual tolerance of 0.5% of the average force in the structure is set. If the force residual is within the tolerance, the configuration is considered to be in equilibrium. Before this configuration is accepted as a converged solution, the analysis also checks that the displacement correction is below 1% of the total incremental displacement. If both the force residual and the displacement correction satisfy the above criteria the solution is accepted as having converged, otherwise the tangent stiffness in the updated configuration (K_{Ta}) is formed and a second iteration carried out

which brings the system closer to equilibrium, Fig. 3. The process is repeated until the solution converges to u_1. Once the solution has been obtained, the load is incremented further and iterations performed to obtain a converged solution for this load increment. Subsequent load increments are carried out until the required load level, F, is reached.

The Newton-Raphson method is a robust solution procedure, generally producing good rates of convergence [14]. However, solutions may fail to converge if local instabilities are present in the model or if the problem exhibits sudden non-linear behaviour, such as structural collapse [15]. One method to overcome local instabilities is to stabilise the model through damping. The commercial solver ABAQUS offers a damped Newton-Raphson procedure in which viscous forces, proportional to the nodal rate of displacement, are automatically added to the model. The damping introduced by this procedure is entirely artificial and serves only to stabilise the solution in the region of any local instabilities. The viscous forces are given by

$$[F_v] = b[M][\dot{u}] \tag{6}$$

where b is the damping coefficient, [M] is the artificial mass matrix (calculated assuming unit density) and $[\dot{u}]$ is the vector of nodal 'velocities' given by $[\dot{u}] = [u]/\Delta t$ in which $[u]$ is the vector of incremental displacement corresponding to a time increment of Δt. Hence, if a local portion of the model becomes unstable the local 'velocities' increase, causing an increase in the viscous forces acting on this region, thus stabilising the model. The equilibrium equation then becomes

$$[F] = [K_T][u] + \frac{b}{\Delta t}[M][u] \tag{7}$$

The damping coefficient, b, is calculated based on the solution of the first increment which is obtained without artificial damping using equation (3). The value of b is chosen such that the resulting viscous damping energy is a small fraction of the strain energy of the model calculated for the first increment, less that 1%. The damping coefficient remains constant throughout the analysis.

3. Validation

This section introduces experimental work carried out to validate the Finite Element analysis methods under development. The experimental programme concentrates on the collapse analysis of fuselage stiffened panels loaded in uni-axial compression. Two sets of experimental compression tests were undertaken:

1. Single Frame Bay Specimen (SFB) – Small scale sub-component specimen consisting of a flat skin stiffened by a single stringer.
2. Multi Frame Bay Specimen (MFB) – Sub barrel panels consisting of a flat skin stiffened by six stringers and two frames.

The small scale SFB specimen test aims to establish the accurate of the six skin-rivet-stringer interface idealisations, Fig. 2. The results of this test programme will feed into the full scale MFB specimen tests, which aim to evaluate the influence of imperfection on the structural response predictions. The following two sub-sections briefly outline the test specimens and test procedures.

3.1. Full Scale MFB Specimen Tests

The full scale MFB specimens consisted of a 0.914 m by 0.864 m skin, stiffened by six stringers and two frame segments as shown in Fig. 4. This configuration gives one representative bay between the two frame segments, with the half bays above and below this serving to introduce the loads into the structure and dissipate undesirable rig end condition effects. The skin extends beyond the end stringers by half the stringer pitch on each side. The frame segments extend past the edges of the panel to enable support fixtures to be attached. The panel was designed such that the failure load was approximately three times the initial buckling load of the skin panels. The rivet pitch was chosen so as to eliminate inter-rivet buckling. The evaluated buckling load, using current empirical analysis methods, predicted local skin buckling at 101 kN and stringer local-flexural failure at 320 kN.

The MFB specimens were tested in a 1,500 kN capacity Avery hydraulic compression testing machine. A 12.7 mm thick Cerrobend (low melting point alloy) base was cast on to the specimens,

producing fully clamped boundary conditions at each end. The ends were subsequently machined flat and perpendicular to the skin to ensure that uniform axial loads were applied. Frame support fixtures were designed to eliminate frame out-of-plane deflections, while allowing axial displacements. The specimens were loaded monotonically in 10 kN steps at a rate of approximately 20 kN/min with the displacement and strains recorded at each increment. The load was increased until specimen failure occurred.

3.2. SFB Specimen Tests

The SFB specimens consisted of a 0.286 m by 0.432 m flat skin, stiffened by a single bulb-tee extruded stringer, as shown in Fig. 5. The skin and stringer material and the skin thickness and stringer dimensions were identical to those of the MFB specimens. The overall dimensions of the specimens were chosen to represent a portion of the MFB specimen consisting of a single stringer attached to the skin, bounded above and below by the frame segments and bounded on either side by adjacent stringers. The evaluated buckling load for the specimen skin was 39.7 kN and the local-flexural failure load for the specimen was 106.5 kN.

The SFB specimens were tested in a 250 kN capacity hydraulic, load-controlled compression-testing machine. As with the MFB specimens, Cerrobend end conditions were applied to the specimens (12.7 mm thick). In addition, edge supports were fitted to the specimen skin edges, the support members were similar to that used by Rothwell [16], consisting of two steel bars separated by a packing strip. The specimen was loaded monotonically at a rate of approximately 10 kN/min until failure occurred, deflection and strain data were recorded automatically at 4-second intervals.

4. Results and Discussion

4.1. SFB Specimen Tests

Fig. 6 illustrates the SFB specimen model. The mesh density is based on the results of the mesh convergence study. The top and bottom rows of elements represent the 12.7 mm of material cast within the cerrobend on either end of the specimen and the two outermost rows of elements

represent the 12.7 mm of skin material constrained by the support bars on either edge. The loads and boundary conditions applied to the model were designed to be as representative of the experimental test as possible, Fig. 6. The resulting load versus end-shortening curves obtained for the computational model with the six different skin-rivet-stringer interface idealisations are shown in Fig. 7 together with the corresponding test data.

Significant errors result by assuming an integral bond between the skin and stringer, with methods (a) and (b) predicting notably higher load carrying capacity than the test specimen, while the four riveted models provide much more accurate structural responses. The other notable feature of these curves is the discrepancy in post buckling stiffness between the test specimen and the Finite Element predictions. It was subsequently discovered that the cause of this discrepancy was the tendency of the edge support bars to separate as skin buckling occurred, with alternate buckles prising the bars apart. This effect essentially reduced the degree of restraint on the edges of the test specimen skin, thus increasing the extent of the skin buckling and hence reducing the post buckling stiffness.

Table 1 details the failure loads and percentage errors based on the experimental load. Due to the separation of the edge support bars during the test the experimental load may be considered a lower bound value. Both integral models, (a) and (b), predict a skin-side failure mode in which yielding occurs on the skin side of the skin-stringer combination with the specimen flexing in the negative Y-direction. All four riveted models, (c) (d) (e) (f), predict a bulb-side failure mode where yielding occurs on the bulb side of the stringer with a corresponding flexure in the positive Y-direction. This difference in failure mode is the reason for the notable difference in post-failure behaviour evident in Fig. 7. The failure modes predicted by the riveted Finite Element models are virtually identical to that exhibited by the test specimen.

Details of the Finite Element solutions are also given in Table 1, comparing the number of analysis increments for method (c) and (e) it is clear that removing the gap elements reduces the

convergence difficulties and hence increases the solution efficiency. It is also clear, comparing (e) and (f), that representing the rivets as a combination of spring elements, as opposed to rigid links, leads to much more problematic solutions, with the number of increments for method (f) being almost double that for method (e).

In light of the results presented above it is clear that, despite the relative efficiency of the integral modelling approaches used in methods (a) and (b), the incorrect failure mode predictions render these idealisations unacceptable for modelling riveted stiffened panels. Following detailed analysis of the axial strain distributions across the skin and stringer [2], the combination of spring elements used in methods (d) and (f) to model the rivets is insufficient to reproduce the secondary warping effect evident in the test specimen, thus indicating that this idealised joint is much more compliant than the actual riveted connection. Of methods (c) and (e), method (c) is taken to be the most accurate modelling approach, since neglecting the contact conditions between the skin and stringer ignores the restraining effect both components have on each other, thus giving a slight reduction in failure load. Incorporating these contact conditions into the model is more representative of the actual structure; however taking contact into account produces a large run-time penalty, in this case resulting in a 160% increase in run-time. As the reduction in failure load predictions due to neglecting the contact between the skin and stringer is very slight, the greatly reduced run times of method (e) may far outweigh the associated loss of accuracy.

4.2. MFB Specimen Tests

A notable feature of the MFB test specimens was a considerable amount of initial overall out-of-plane distortion due to the residual stresses introduced by the riveting process. Various levels of stress-free overall distortion were incorporated into the analysis to investigate the sensitivity of the structural response to this geometric imperfection.

Fig. 8 illustrates the MFB specimen model; again the mesh density is based on the results of the mesh convergence study, as with the SFB specimen model, loading and boundary conditions

employed, were designed to be as representative of the experimental test as possible. However, while the second order elements, S8R5, gave the most efficient solution for the SFB specimen analysis, the full scale MFB specimen model encountered convergence difficulties during the solution. The analysis therefore required more increment step, resulting in a relatively inefficient model. A first order elements model consisting of ABAQUS S4R shell elements [10] with approximately the same number of Degrees Of Freedom (DOFs) as the second order model provided an efficient solution, reaching the applied end-shortening without encountering convergence difficulties. For multi frame bay structures, second order elements may be expensive, with the solution failing to converge quickly. For such models first order elements should be used.

The load versus end-shortening curves for the MFB specimen model with component interface idealisation methods (c) and (e) are shown in Fig. 9, together with the corresponding test data. For both analyses the initial imperfection was in the shape of the fundamental buckling mode with a maximum magnitude equal to 10% of the skin thickness. The predicted structural responses are similar in both cases, however there are significant differences between both models in the region of skin panel buckling and approaching specimen failure.

The central skin bay buckling modes predicted at failure for method (c) and (e) were different. The model without gap elements, method (e), exhibited three longitudinal buckles whereas the model with gap elements, method (c), exhibited four longitudinal buckles. It is this difference in buckling mode between both models together with the increase in restraint offered by the addition of gap elements that leads to the discrepancies in the load versus end-shortening curves. The failure modes obtained from both models are similar, with skin-side failure predicted, however the test specimens experienced bulb-side failure modes, Fig. 10. The corresponding failure loads along with solution details are given in Table 2.

The addition of gap elements makes convergence more difficult, Table 2. The increase in number of increments plus the larger run times per increment leads to a total run-time approximately 2.5

times larger than for the same model without gap elements. However, it should be noted here that, for imperfection sensitive structures, the addition of gap elements may induce a change of buckling mode which may, in turn, lead to a reduction in buckling loads and/or failure load. Thus it is conceivable that, in certain cases, the addition of gap elements at the component interfaces may lead to lower buckling and or failure load predictions.

As mentioned earlier both test specimens exhibited a considerable amount of initial out-of-plane distortion due to residual stresses introduced by the riveting process. This distortion was in the negative Z-direction, Fig. 8, with a magnitude of approximately 2 mm mid way along the specimens. To investigate the effects of this distortion, overall imperfections with magnitudes of 0.254, 1.016, 2.032 and 2.540 mm were incorporated into the model with component interface idealisation method (c). These imperfections were assumed to be sinusoidal in nature, represented by equation (8).

$$w_0 = A \cdot \sin \frac{\pi Y}{863.6} \tag{8}$$

Eigenvalue analysis of the specimen model was carried out to determine the fundamental skin panel buckling modes which were subsequently used as initial local imperfections, with a magnitude of 10% of the skin thickness.

The resulting load versus end-shortening curves, together with the baseline case with no overall imperfection, are shown in Fig. 11, in which A corresponds to the overall imperfection magnitude. While the pre and early post buckling structural responses are almost identical for all five analyses, the predicted load carrying capacity is highly sensitive to the magnitude of the initial overall imperfection. This is due to the fact that as the applied load is increased, with the presence of these overall imperfections, corresponding overall out-of-plane deflections develop in the negative Z-direction thus increasing the compressive stresses in the bulb-side of the stringers and promoting (bulb-side) specimen failure. The larger the overall imperfection magnitude, the greater the out-of-plane deflections and bulb-side compressive stresses and, hence, the lower the failure load, Fig. 11.

The central skin bay buckling mode predicted at failure consisted of three longitudinal buckles in each case. As suggested by the rapid post failure unloading evident in Fig. 11, overall imperfection models predicted a bulb-side failure mode very similar to that shown in Fig. 12. Table 3 gives the predicted failure loads and percentage errors based on the minimum experimental failure load. These values clearly demonstrate the high degree of sensitivity to overall imperfections. With an overall imperfection magnitude of 2.54 mm leading to a reduction in failure load of approximately 16% from that of the baseline model with no overall imperfection. The correlation to the minimum experimental failure load is excellent with the measured overall imperfection of 2.032 mm included, however it should be noted here that this value is an approximate measurement and the exact nature of the overall imperfection of the test specimens is unknown.

While substantial initial overall imperfection were present in both test specimens, equivalent imperfections would not develop in actual fuselage structures; the frames prevent radial deflection of the stringers at the attachment points, with the only possible deflections occurring between frames, however the frames are sufficiently close together to ensure that these deflections are minimal. Nonetheless, from a test-analysis correlation point of view, these results clearly indicate that any notable overall imperfection present in test specimens must be correctly reproduced in the FE model to enable accurate predictions of the post buckling response.

5. Conclusion

5.1 Conclusions

The work presented herein contributes to the development of Finite Element methods for the accurate prediction of the post buckling behaviour of conventional aircraft fuselage panels subjected to varying combinations of axial and shear loading. The presented work focused on flat riveted panels subjected to uniform axial compression. Listed below are a series of guidelines for the Finite Element analysis of flat riveted panels subjected to uniform axial compression. The guidelines are refined for the above structures only. Due to numerous factors affecting Finite

Element predictions, it is necessary to carry out element / mesh / idealisation / imperfection / solution procedure studies relevant to the class of structure being studied.

Elements – Quadratic shell elements provide the most efficient and accurate solution for small sub-component models. For larger panel structures with multiple stiffeners linear shells provide a more robust solution and with sufficient mesh refinement will lead to accurate failure predictions.

Meshes – When using quadratic shell elements mesh convergence studies indicate that panel skin, stringer flange and stringer web may be accurately modelled using a minimum of four elements per buckle half wavelength (nine nodes).

Idealisation – A number of different idealisations of skin-rivet-stringer interface have been examined, and it has been found that riveted panels cannot be modelled as integral structures. The rivets must be modelled as discrete connections, with separation of the components allowed to occur away from the rivet locations. The developed approach models the rivets as rigid links with gap elements simulating the contact between the panel sub-components.

Imperfections – Initial overall imperfections can significantly affect the structural response predictions, with the failure load being particularly sensitive. While such imperfections, in general, do not occur in actual fuselage structures, they may occur in test specimens hence, from a test-analysis correlation perspective, any notable overall imperfection should be correctly reproduced in the analysis model.

Solution Procedures – It has been shown that, with appropriate level of artificial damping that the damped Newton-Raphson procedure may be used to predict post buckling and collapse behaviour of large complex models.

5.2 Future Work

Typically imperfections occur as a result of residual stresses generated during the riveting process, these residual stresses must also be modelled with in Finite Element analysis along with the geometrical imperfections. The application of the analysis methodology developed here must be extended to first flat stiffened panels subjected to uniform shear loading and then to combined loading, before being extended to cover the more representative problem of curved panels [17]. Finally, a concern with the modelling and analysis procedure detailed above is the time required to perform a complete analysis [18]. For the large specimen analysis complete analysis times on a SUN Enterprise^{TM} 3500 with six 400 MHz UltraSPARC II^{TM} processors and 6 GB of RAM was in the region of 16 hours.

Acknowledgements

The authors wish to thank the Industrial Research and Technology Unit (IRTU–ST-198) for their financial assistance, as well as Gary Moore, Ken Poston and Derek Cottney for their technical support.

References

1. Niu M C. Airframe Structural Design. 1st edition, Hong Kong Conmilit Press Ltd, 1988.
2. Lynch C J. A Finite Element Study of the Post buckling Behaviour of a Typical Aircraft Fuselage Panel. PhD Thesis, Queen's University Belfast, Belfast, N. Ireland, 2000.
3. NASA, NASA Astronautics structures manual, Volume 3, NASA, Washington, US, 1961.
4. ESDU Structures sub-series, Engineering Sciences Data Units, ESDU International Ltd.
5. Niu M C. Airframe Stress Analysis and Sizing. 2nd edition, Hong Kong Conmilit Press Ltd, 1999.
6. Bruhn E F. Analysis and Design of Flight Vehicle Structures. 1st edition, Tri-State Offset Company, 1973.
7. Timoshenko S P, Gere J M. Theory of elastic stability, 2nd edition, McGraw-Hill Book Company Inc., 1961.

8. Ramberg W, Osgood W R. Description of stress-strain curves by three parameters, NACA-TN-902, NACA, 1943.
9. Bulson P S. The stability of flat plates, 1st edition, Chatto & Windus, London, 1970.
10. Anonymous. ABAQUS / Standard User's Manual. Version 6.1, Hibbitt, Karlsson and Sorenson, 2000.
11. Domb M M, Elliott W G, Leigh B R. Modelling of stiffener Crippling Phenomena Using Finite Element Analysis. Canadian Aeronautics and Space Journal, Vol. 44, No. 4, pp 256-262, 1998.
12. Hu S Z, Jiang L. A Finite Element simulation of the test procedure of stiffened panels, Volume 11 pp 75-99, Marine structures, 1998.
13. Wittenberg T C, van Baten J J, de Boer A. Design of fibre metal laminates shear panels for ultra-high capacity aircraft, Volume 4 pp 99-133, Aircraft Design, 2001.
14. Becker A A. Understanding non-linear finite element analysis - Through illustrative benchmarks, 1st edition, NAFEMS (ISBN 1-8743-7635-2), 2001.
15. Anonymous. ABAQUS training course note - Obtaining a converged solution with ABAQUS, Hibbitt, Karlsson and Sorenson Inc., 1999.
16. Rothwell A. An experimental investigation of the post-buckling efficiency of Z-section stringer-skin panels, Volume 85 pp 29-33, Aeronautical journal, 1981.
17. K. Koffi, A. Gibson, M. Price. A comparison of FE buckling analysis predictions and experimental results for riveted aircraft fuselage panels, Tenth international conference on computational methods and experimental measurements, Alicante, Spain, 2001.
18. Murphy A, Price M, Gibson A, Armstrong C G. Efficient non-linear modelling of fuselage panels, ICAS-2002-3.2.1, ICAS 2002, Toronto, Canada, 2002.

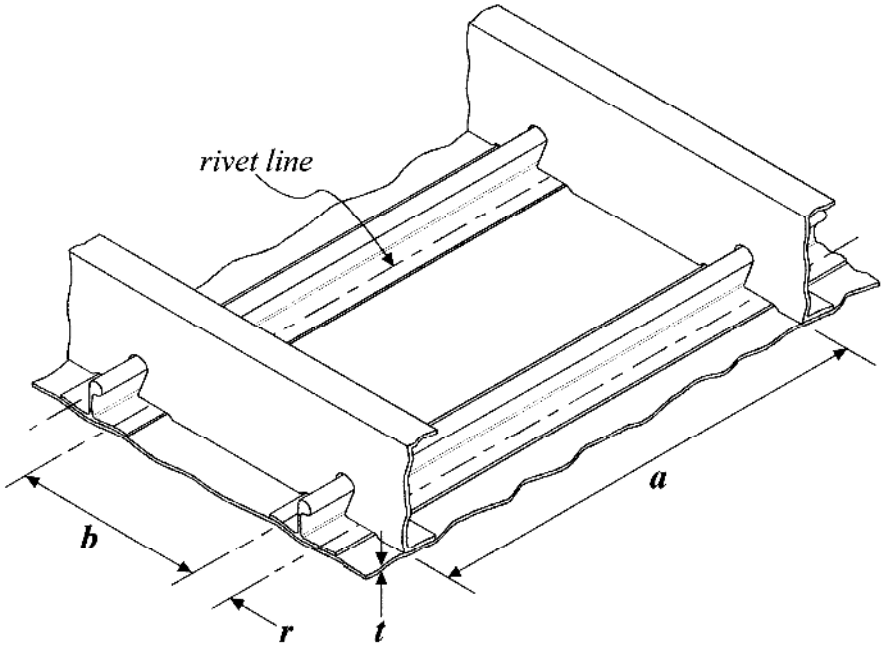

Fig. 1. Dimensions used to calculate local skin panel buckling stress.

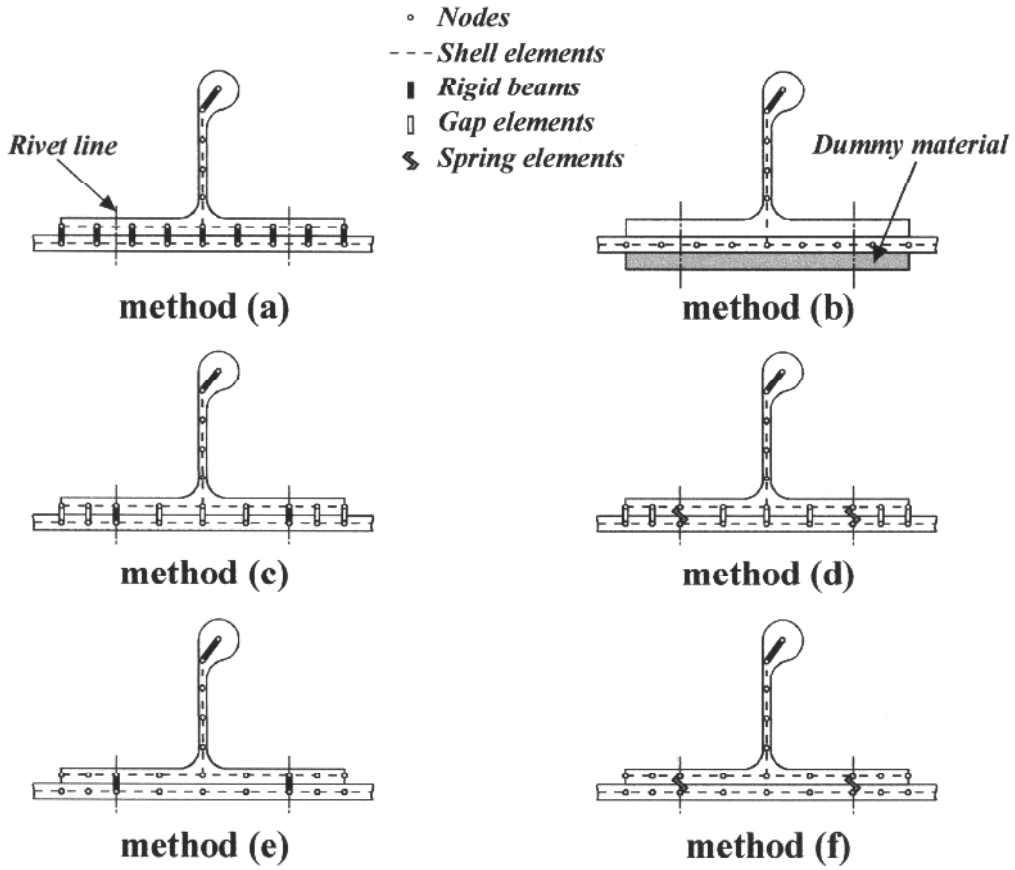

Fig. 2. Skin-rivet-stringer interface idealisation.

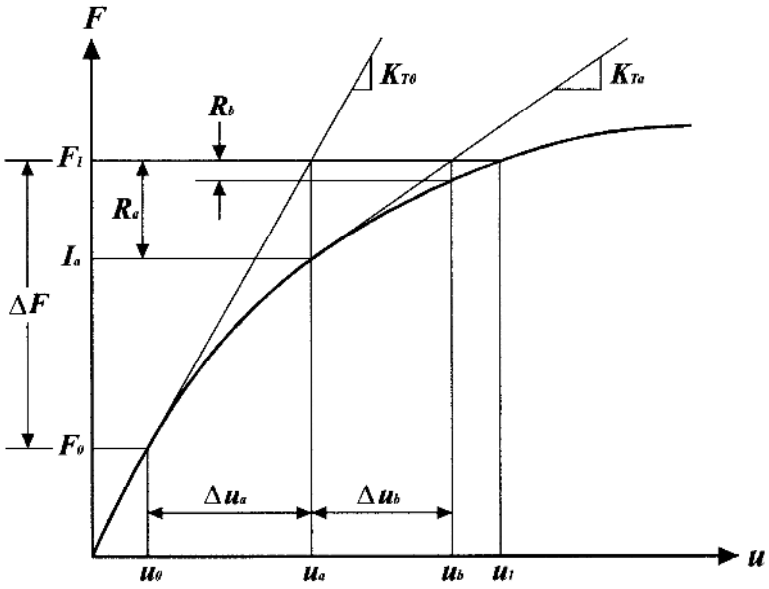

Fig. 3. A load increment carried out using the Newton-Raphson solution procedure.

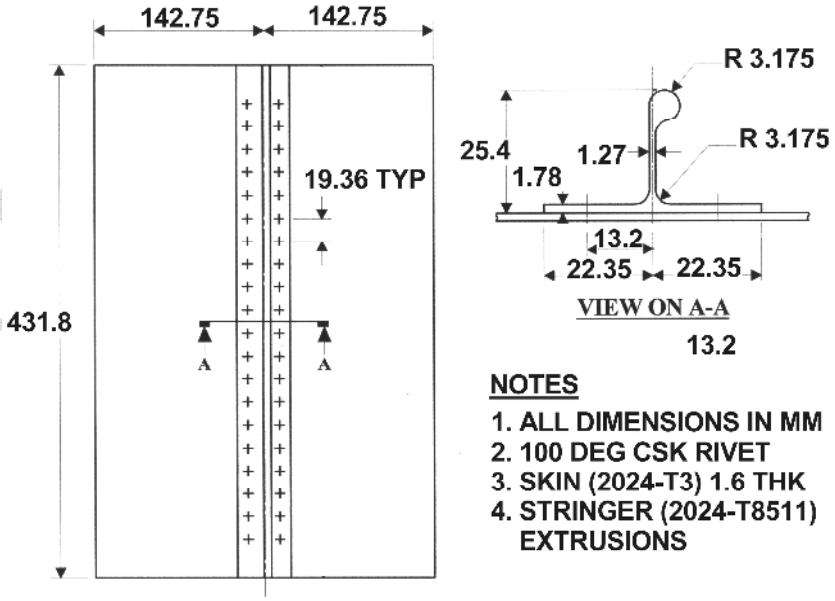

Fig. 5. Small scale SFB specimen.

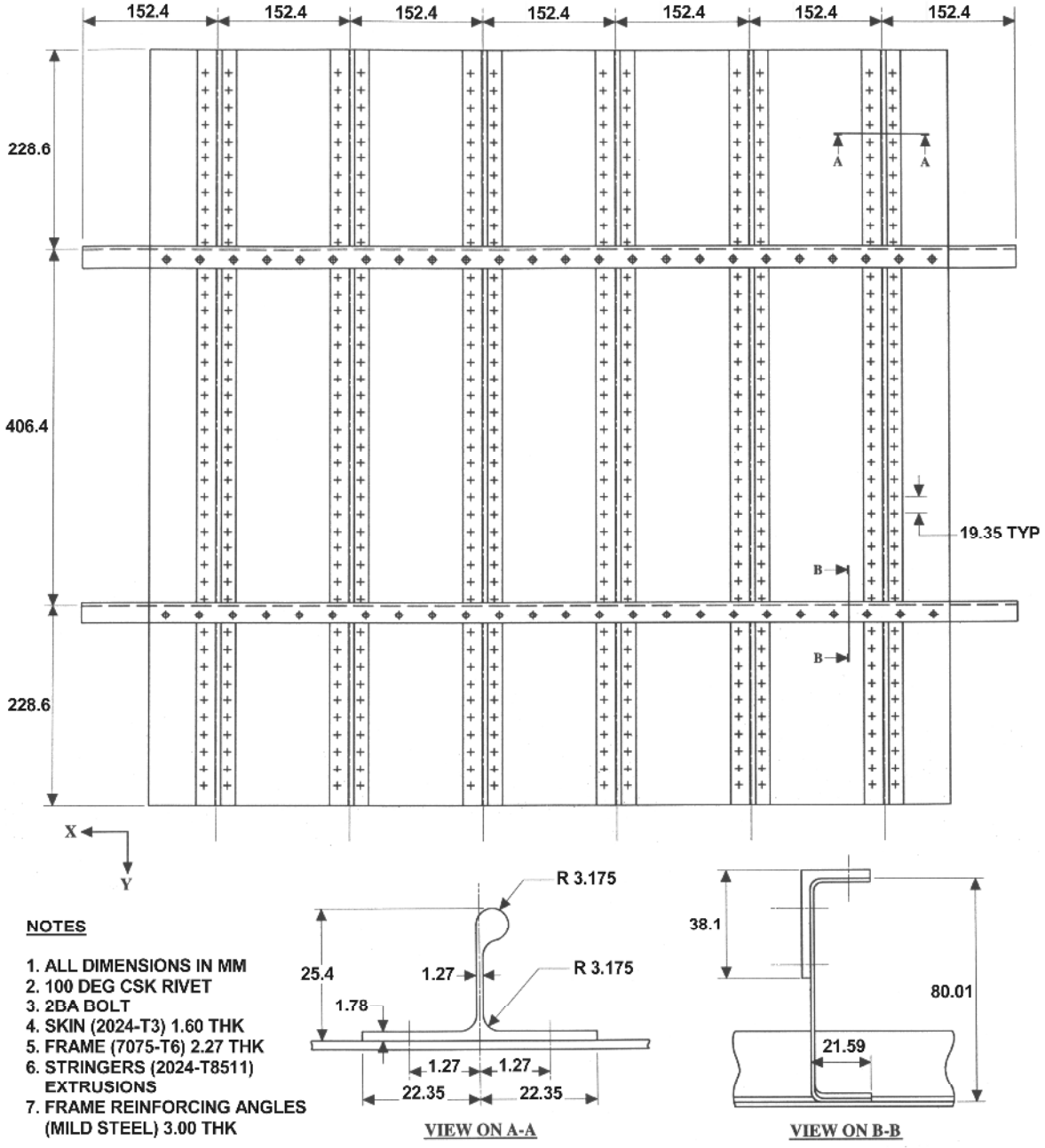

Fig. 4. Full scale MFB specimen.

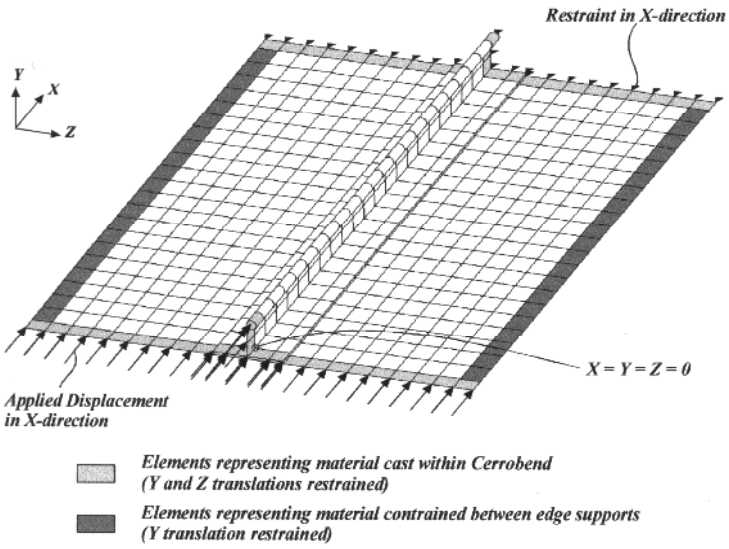

Fig. 6. SFB specimen model (Second order elements).

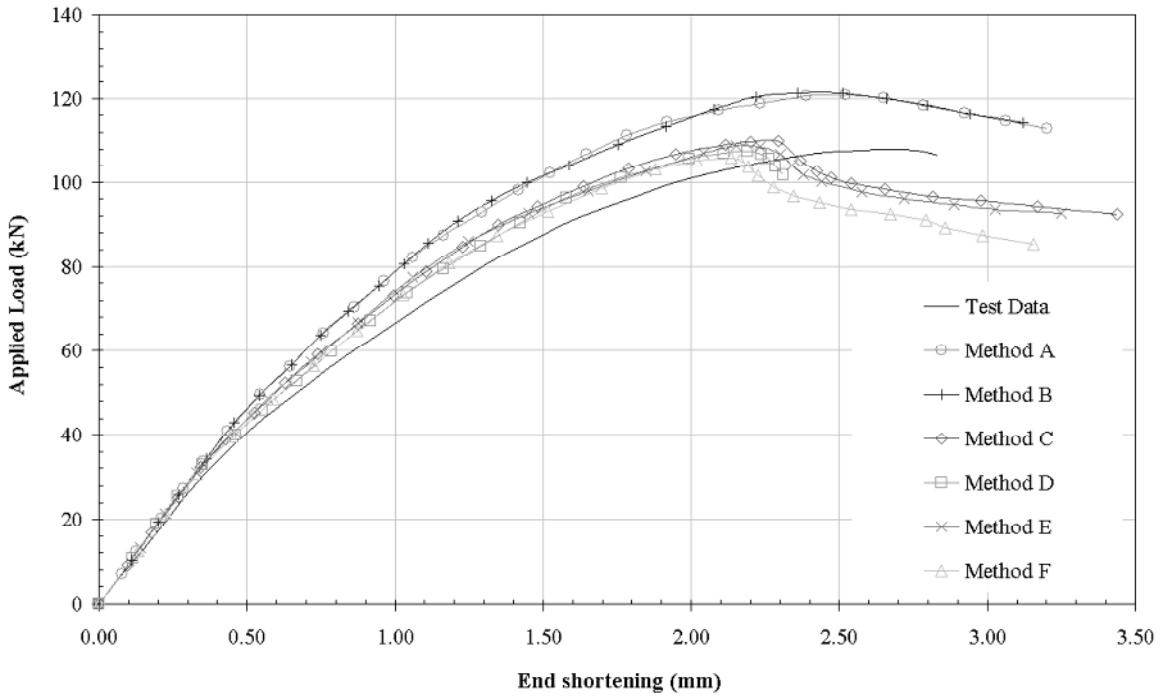

Fig. 7. Experimental/computational load versus end-shortening curves for the SFB specimen.

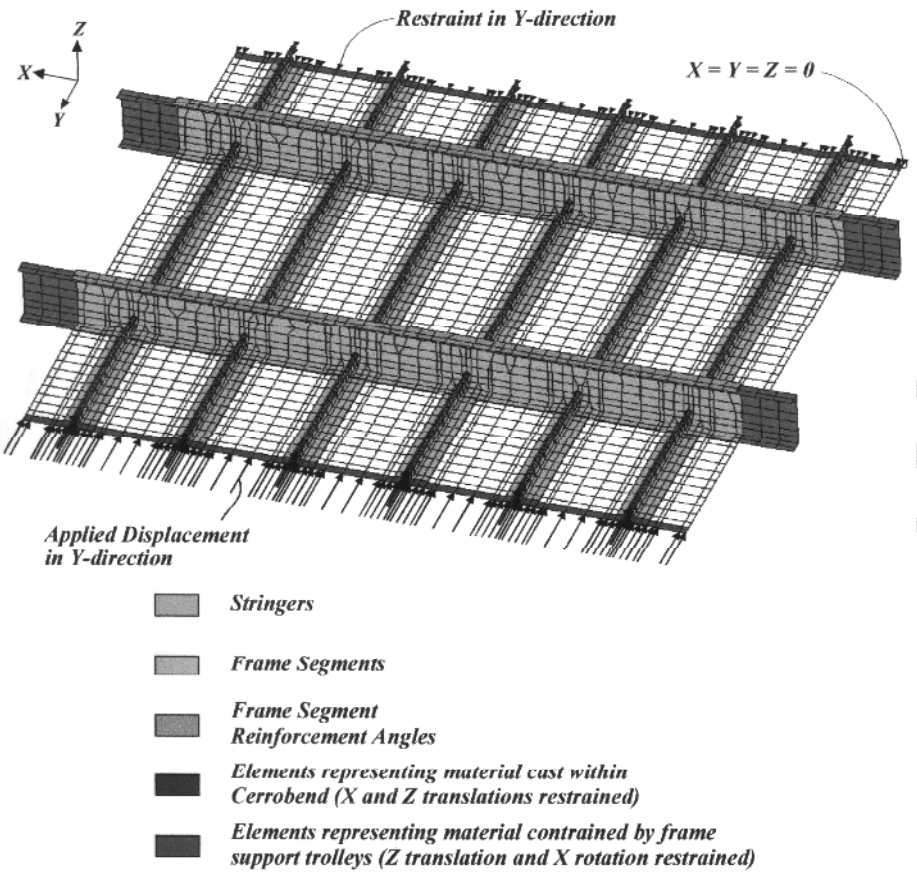

Fig. 8. MFB specimen model (Second order elements).

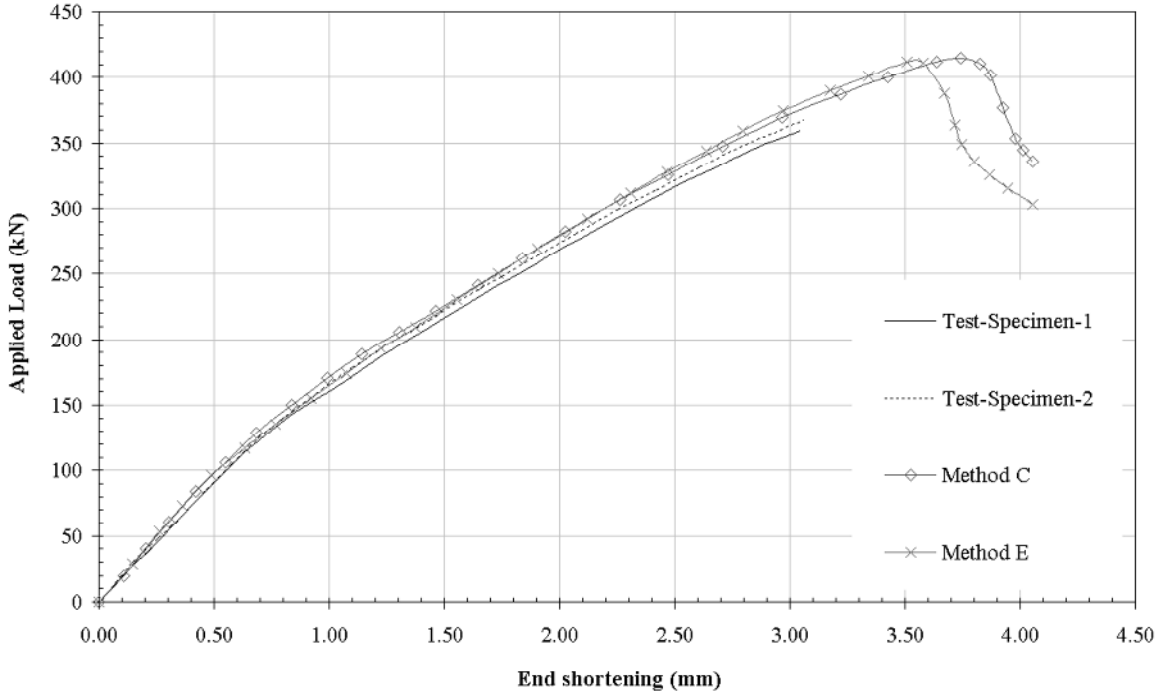

Fig. 9. Experimental/computational load versus end-shortening curves for the MFB specimen.

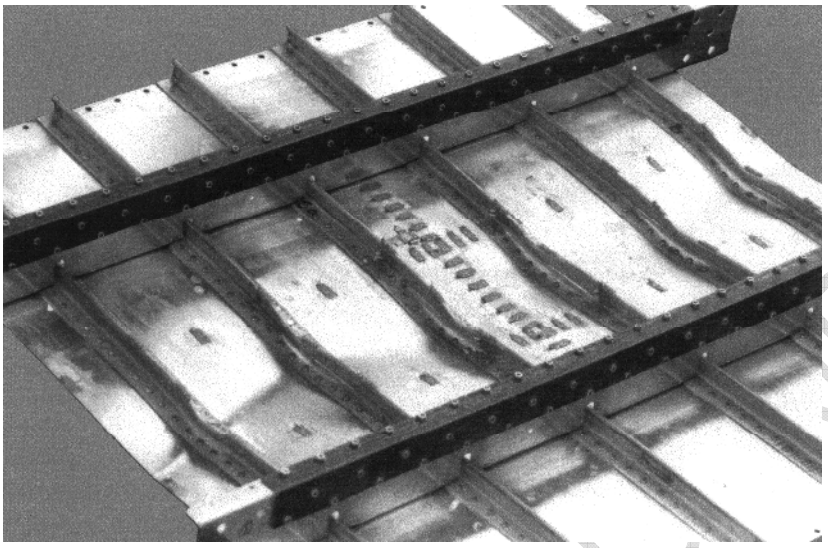

Fig. 10. Bulb-side failure mode of MFB Test-Specimen-2.

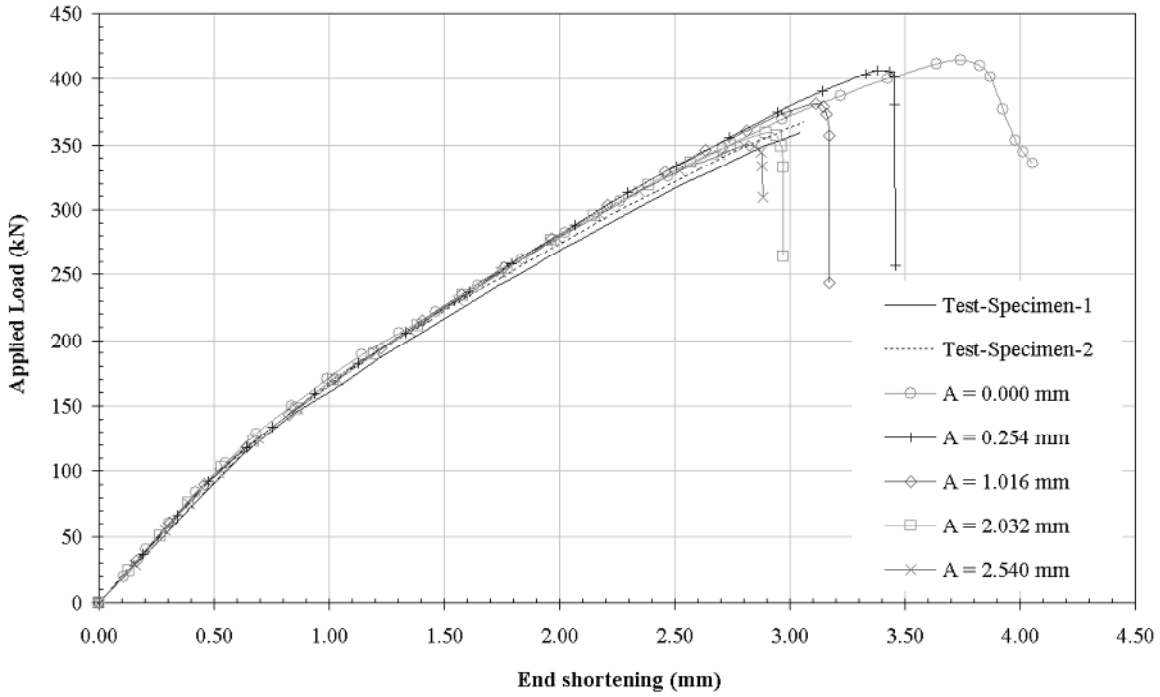

Fig. 11. Experimental/computational load versus end-shortening curves for the MFB specimen with initial global geometry imperfection.

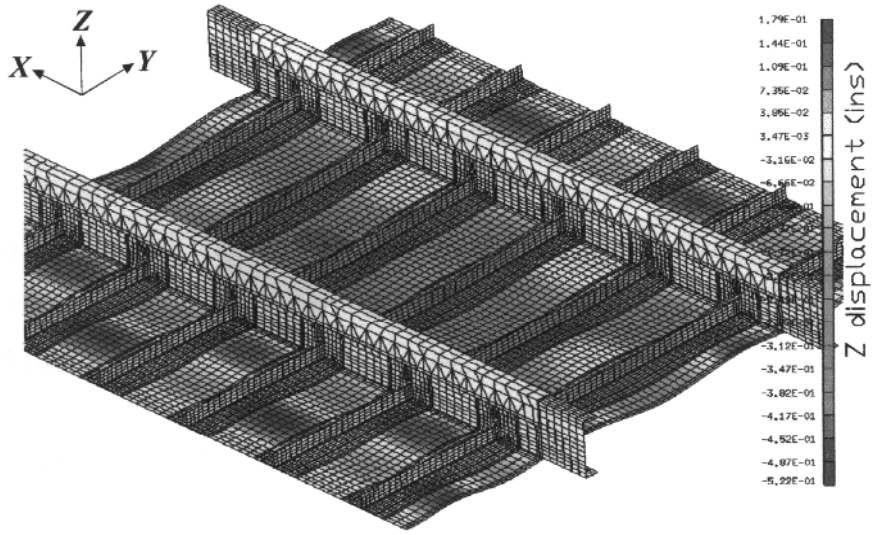

Fig. 12. Bulb-side failure mode obtained with an initial overall imperfection (Magnitude = 2.032 mm)

	Failure Load (kN)	Percentage Error (%)	Number of Analysis Increments	Increment Run Time (Secs)
Test	**108.1**	**---**	**---**	**---**
Method (a)	120.8	11.7	13	27
Method (b)	121.6	12.5	14	23
Method (c)	109.8	1.6	23	60
Method (d)	107.5	-0.5	31	56
Method (e)	108.7	0.6	15	35
Method (f)	106.1	-1.9	29	35

Table. 1. Failure loads plus analysis costs for the SFB specimen.

	Failure Load (kN)	Percentage Error* (%)	Number of Analysis Increments	Increment Run Time (Secs)
Test-Specimen-1	**363.7**	**---**	**---**	**---**
Test-Specimen-2	**373.7**	**---**	**---**	**---**
Method (c)	414.4	14.0	51	1164
Method (e)	412.1	13.3	43	543

** - Based on lower bound test value (Test-Specimen-2)*

Table. 2. Failure loads plus analysis costs for the MFB specimen.

	Failure Load (kN)	Percentage Error* (%)
Test-Specimen-1	**363.7**	**---**
Test-Specimen-2	**373.7**	**---**
A = 0.000 mm	414.4	14.0
A = 0.254 mm	407.0	11.9
A = 1.016 mm	380.8	4.7
A = 2.032 mm	359.2	-1.2
A = 2.540 mm	349.5	-3.9

** - Based on lower bound test value (Test-Specimen-2)*

Table. 3. Failure loads for the MFB specimen models with overall imperfections.